Cellular Uptake, Cytotoxicity, and Innate Immune Response of Silica–Titania Hollow Nanoparticles Based on Size and Surface Functionality

Wan-Kyu Oh, Sojin Kim, Moonjung Choi, Chanhoi Kim, Yoon Seon Jeong, Bo-Ram Cho, Ji-Sook Hahn, and Jyongsik Jang*

School of Chemical & Biological Engineering, Seoul National University, 599 Gwanangro, Gwanak-gu, Seoul 151-742, Korea

ABSTRACT Silica–titania hollow nanoparticles (HNPs) with uniform diameters of 25, 50, 75, 100, and 125 nm were fabricated by dissolution and redeposition method in order to evaluate size dependent cellular response. Surface-modified HNPs with cationic, anionic, and neutral functional group were prepared by silane treatment. We systematically investigated cellular internalization, toxicity, and innate immune response of HNPs in human breast cancer (SK-BR-3) and mouse alveolar macrophage (J774A.1) cells. Size- and surface functionality-dependent cellular uptake of HNPs was investigated by fluorescence labeling (fluorescein isothiocyanate), inductively coupled plasma-emission spectroscopy, and ultrastructural resolution using transmission electron microscopy. Viability, reactive oxygen species, and apoptosis/necrosis of HNP-treated J774A.1 revealed the size-dependent phenomenon. Innate immune response of HNP-treated macrophages was measured by three cytokines such as interleukin-1, interleukin-6, and tumor necrosis factor α. Among the HNPs of different sizes, 50-nm HNPs demonstrated the highest toxic influence on macrophages. Among the HNPs with surface functionalities, cationic HNPs demonstrated the most toxic effect on J774A.1 and the highest uptake efficiency. The toxicity results of HNP-treated macrophages were consistent with the cellular internalization efficiency. These findings provide size- and surface functionality-dependent nanotoxicity and uptake of HNPs, and lead to HNPs for bioapplications such as drug delivery and imaging probe.

KEYWORDS: cytotoxicity · cellular uptake · immune response · hollow nanoparticles · surface functional group · size dependence

Recent progress in synthesis of nanoparticles has enabled the preparation of nanometer-sized materials with controlled structures and functionalities.[1,2] Nanomaterials have attracted great attention for various biomedical applications such as drug delivery and cellular imaging because of their fascinating physicochemical properties.[3−5] Nanostructured materials exhibit superior bioactivity by exponential increase of surface area and alteration in the physicochemical and structural properties with a decrease in their diameters.[6,7] Furthermore, specific surface groups including hydrophilic, hydrophobic, lipophilic, and lipophobic could function as reactive sites.[8] However, these functional groups can induce harmful effects to biological systems mainly owing to their oxidative stress and inflammatory response.[9] For instance, electron capture on the surface of nanoparticles can lead to the formation of superoxide radical ($O_2^{\bullet-}$), resulting in generating additional reactive oxygen species due to Fenton chemistry and dismutation.[10,11] Nevertheless, there are limited researches concerning size- and surface functionality-dependent nanotoxicity on biological systems. In the case of biomedical applications, the nanoparticles of different diameters and surface functionalities should be evaluated systematically from a cytotoxic viewpoint.

For cancer therapy, the synthesis of nanoparticles with void structure is a crucial issue in order to deliver the drug efficiently in aqueous solution.[12] The void space of hollow nanoparticles has been successfully applied for encapsulation and controllable release of biochemical molecules such as drug, DNA, and dyes.[13,14] Therefore, hollow nanoparticles have received considerable attention in fabrications and applications.[15−17] Among various fabrication methods of hollow nanoparticles, the sacrificial template method and the template free method have emerged as promising candidates for the optimal synthetic way.[18] For instance, the Kirkendall effect and Ostwald ripening have been used for the fabrication of versatile nanostructures from nanotubes to hollow nanoparticles.[19] A novel synthetic method of producing hollow nanoparticles has provided opportunity for versatile application *via* modulating mechanical, optical, electrical, and chemical properties.[20,21] However, it is necessary to prepare nonagglomerated and uniform

*Address correspondence to jsjang@plaza.snu.ac.kr.

Received for review March 18, 2010 and accepted August 04, 2010.

Published online August 10, 2010. 10.1021/nn100561e

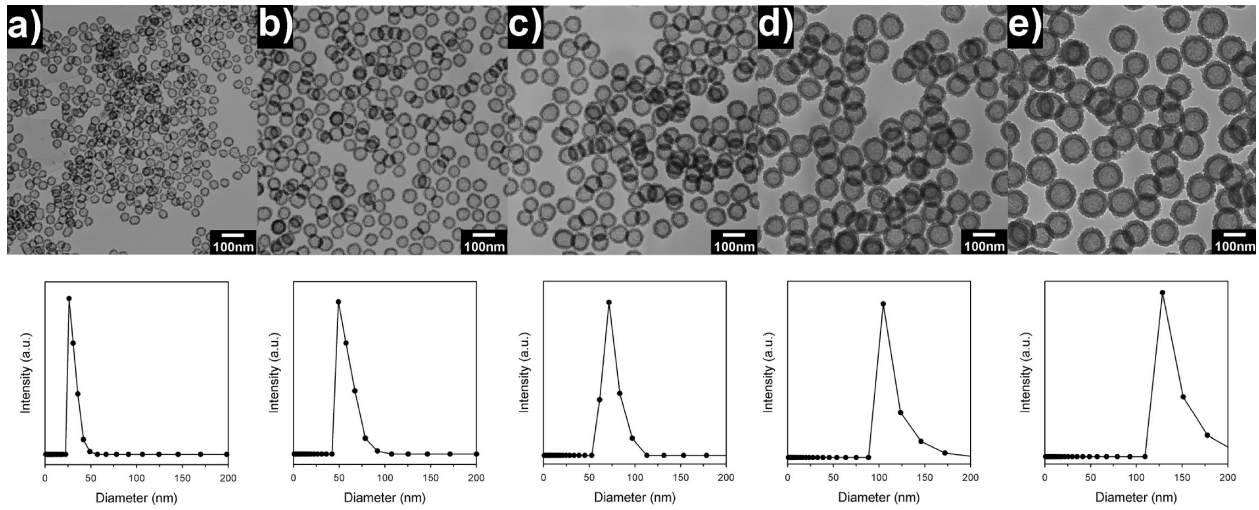

Figure 1. TEM images of HNPs of five different diameters and their corresponding size distribution by using ELS: (a) HNP25, (b) HNP50, (c) HNP75, (d) HNP100, and (e) HNP125.

hollow nanomaterials with controllable diameter in the nanometer regime.

Here, we report the fabrication for monodisperse silica−titania hollow nanoparticles (HNPs) with diameters of 25, 50, 75, 100, and 125 nm and surface functional groups of amine, carboxylate, and methylene. We systematically investigate the key factors affecting cellular uptake, cytotoxicity, and innate immune response of HNPs with size- and functionality-dependence in human breast cancer SK-BR-3 and mouse alveolar macrophage J774A.1 cells. The cellular internalization of HNPs toward SK-BR-3 and J774A.1 was analyzed by fluorescence labeling (fluorescein isothiocyanate), inductively coupled plasma-emission spectroscopy, and ultrastructural alteration using transmission electron microscopy. The cellular effects of HNPs-treated J774A.1 on ATP production, oxidative stress, apoptosis/necrosis, and innate immune response were measured in order to scrutinize the toxicity of silica−titania hollow nanoparticles based on size and surface functionality.

RESULTS AND DISCUSSION

Fabrication and Characterization of HNPs. Hollow nanoparticles (HNPs) were evolved from silica−titania core−shell nanoparticles (CSNPs) as starting materials prepared by dissolution and redeposition of silica. First, CSNPs were obtained from introduction of titania layer onto the surface of silica nanoparticles. (see Materials and Methods).[22] In particular, ammonium ions played a role in providing electrostatic interaction between titania precursor (titanium tetraisopropoxide; TTIP) and the surface of silica nanoparticles as well as offering a catalyst for the synthesis. Under basic solution, the hollow nanostructures were transformed from the as-prepared core−shell nanostructures through the reversible process of dissolution of silica (core part) and redeposition on the surface of the nanoparticles. This morphological change occurs because the hydroxide ion of the basic sodium hydroxide solution can dissolve silica by coordinating to silicon atoms and weakening siloxane bonds.[17,23]

Figure 1 illustrates representative transmission electron microscopy (TEM) images of HNPs with controllable diameter and electrophoretic light scattering spectrophotometer (ELS) curves of the HNPs with different diameters. Remarkably, the TEM images of HNPs revealed uniform diameters of 25, 50, 75, 100, and 125 nm (denoted HNP25, HNP50, HNP75, HNP100, and HNP125, respectively). The ELS curves exhibited narrow size distribution that could be applicable to research for size-dependent toxicity. The dispersibility of the HNPs was validated by a well-dispersed solution with HNPs at 200 mg mL^{-1} after one year, and this result was considered to be favorable in biomedical applications. Furthermore, these properties can provide a clear understanding of cellular response with nanoparticles with different physical parameters.

In addition, surface functionality could be a key factor in cellular response. Therefore, aminated, carboxylated, and methylated hollow nanoparticles with diameters of 50 nm were prepared by silane modification (3-aminopropyltriethoxysilane, carboxyethylsilanetriol sodium salt, and 3-methacryloxypropyltrimethoxysilane, respectively) and were designated by A-HNP50, C-HNP50, and M-HNP50. The successful introduction of different surface functionalities was proved by FTIR (Figure 2). A-HNP50 had the asymmetric amines stretching broad peak at 3450 cm^{-1}, indicating that the aminated surface functional groups were introduced. M-HNP50 exhibited the C═O stretching vibration at 1730 cm^{-1}. However, other bands from propyl chain and C−O chain were not observed due to the strong Si−O band. Similarly, in the case of C-HNP50, C═O bands also were shown, but the asymmetric carboxylic acid salts stretching peak at 1540 cm^{-1} could be a different peak for M-HNP50. In addition, zeta potential results suggested

the different surface functionalities (Supporting Information, Table S1). Cationic aminated functional groups increased the zeta potential value, and the lower value was observed in the anionic carboxylated hollow nanoparticles. M-HNP50 had the similar value of zeta potential compared to pristine HNP50.

Cellular Uptake of HNPs. To quantify the internalized HNPs into the SK-BR-3 and J774A.1 cells, fluorescein isothiocyanate (FITC) labeling on the HNPs (termed FITC-HNP) was performed *via* covalent linking between FITC and the HNPs (see Materials and Methods). Figure 3 represents the flow cytometry analysis of SK-BR-3 and J774A.1 cells incubated with 25 μg mL^{-1} FITC-HNPs for 24 h. About 4−6 fold increase in the fluorescent intensity of HNP50-internalized SK-BR-3 and J774A.1 was observed distinct from that of HNP125-internalized SK-BR-3 and J774A.1. Distinct peaks of high fluorescent intensity were observed with HNP50- and HNP75-internalized cells, but lower fluorescent intensity from cells incubated with HNP25-, HNP100-, and HNP125-internalized cells. These latter cells had an emission spectrum near the control. Generally, the median value is considered to be the number of particles associated with the cells and show the cellular uptake.[24] Therefore, the cellular uptake was in order of HNP50 > HNP75 > HNP25, HNP100 > HNP125.

The live cell microscopic images of SK-BR-3 and J774A.1 cells incubated with 10 μg mL^{-1} FITC-HNPs are shown in Figure 4. Live cell microscopic images could be the clear demonstration tools for cellular uptake of the HNPs with different diameters. Both cell lines with HNPs had no considerable change in cell shape. Green fluorescence that represented signal from FITC was observed inside and outside of the both cell lines. From the intensity and distribution of the FITC-HNPs, it is considered that the number of the HNPs was taken up into cells. Among different sizes of the HNPs, HNP50 and HNP75 exhibited a higher uptake ratio than other HNPs in both cell lines, which was consistent with flow cytometry results. Moreover, this result was consistent with the findings of Huang *et al.* that 70-nm SiO_2 nanoparticles could translocate into the nucleoplasm of HepG2 cells.[25] In the case of J774A.1, the quantity of cellular HNPs was larger than that in SK-BR-3, probably due to phagocytosis.

To compare the uptake efficiency of the HNPs quantitatively, HNP-treated cells were also measured by the titanium amount *via* inductively coupled plasma-emission spectrometer (ICP). The HNP-treated cells were mixed with HF and HNO_3 in aqueous solution to allow dissolution of the titanium. The results show that the mass of titanium per cell is related to the size of HNPs (Figure 5). The cellular uptake ratio is particle-size-dependent in the order 50 ≥ 75 > 100 > 125 > 25 nm. The uptake of HNP50 was approximately 1.3−1.7 times than that of HNP125. The optimal sizes, 50 and 75 nm, for cell uptake are consistent with the cell uptake

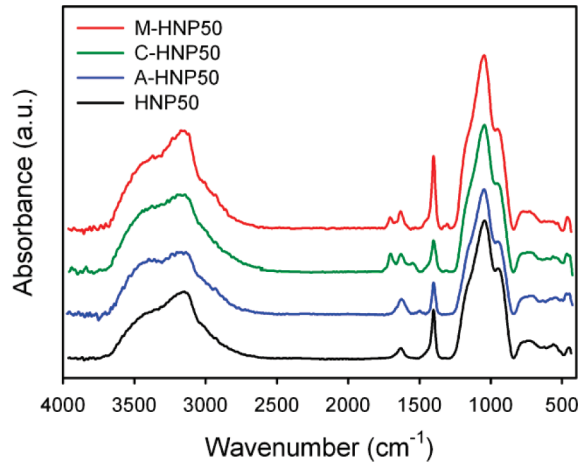

Figure 2. FTIR spectra of surface-functionalized HNPs.

of other particles recently reported, which demonstrated that 50-nm glycovirus entered cells *via* receptor-mediated endocytosis more efficiently than smaller nanoparticles.[26] In addition, Huang *et al.* has also found that 70-nm SiO_2 nanoparticles could translocate into the nucleoplasm of HepG2 cells.[25] Besides, surface functionality provided the strong effect on cellular uptake, resulting in A-HNP50 represented higher uptake ratio than other functionalized HNPs. The cellular uptake efficiency of A-HNP50 was 1.30−1.75 times higher than that of C-HNP50, which originated from electrostatic interaction between the cationic surface charge of nanoparticles and the negative charge of the cell membrane.

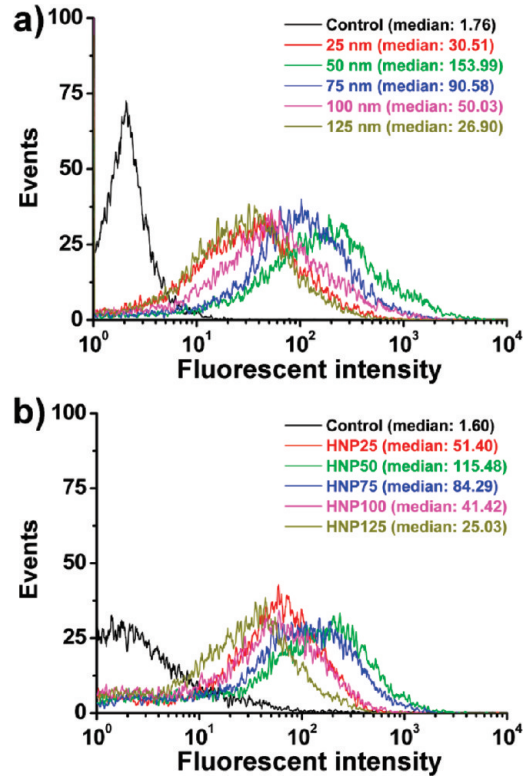

Figure 3. Flow cytometric analyses of (a) SK-BR-3 and (b) J774A.1 cells incubated with FITC-HNPs for 24 h.

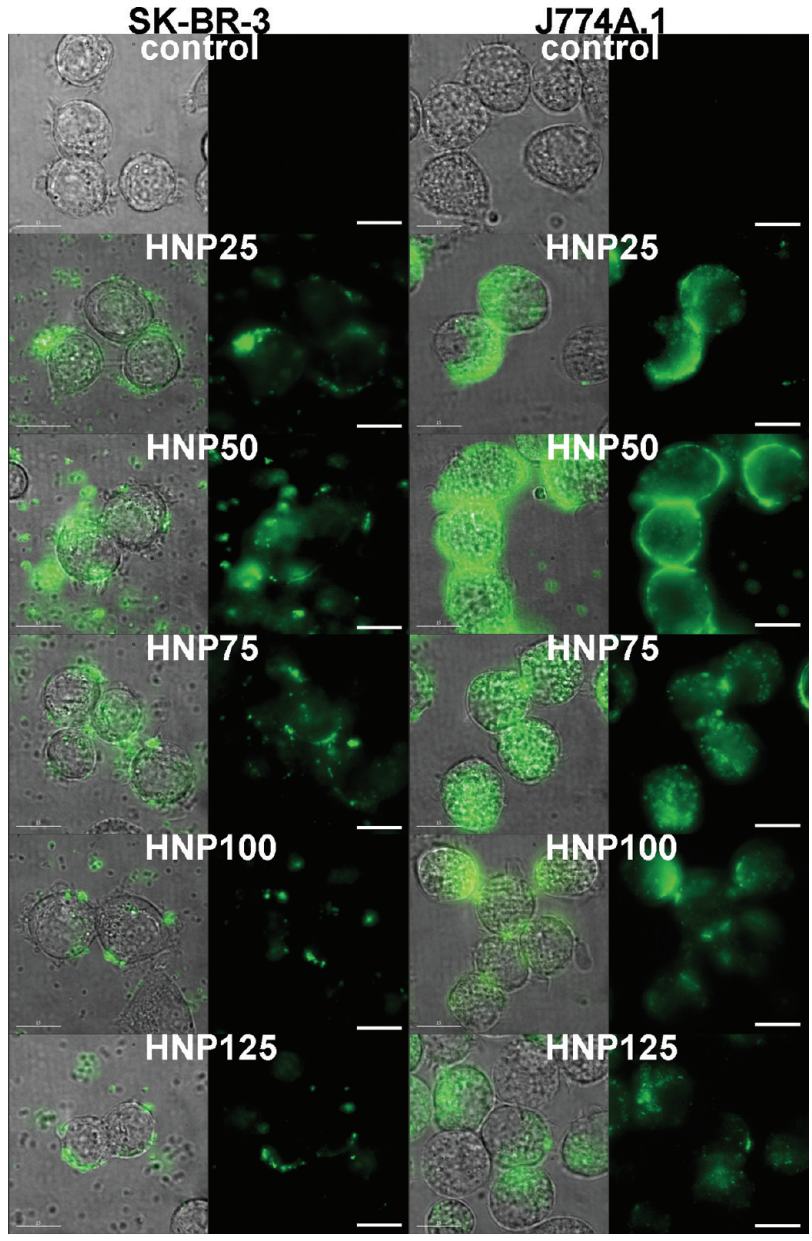

Figure 4. Live cell differential interference contrast (DIC) and fluorescent images of FITC-tagged HNP-treated SK-BR-3/J774A.1 cells (10 μg mL^{-1}); negative control, HNP25, HNP50, HNP75, HNP100, and HNP125. DIC images were taken at the same time corresponding to the cells. Scale bars = 15 μm.

This result was also consistent with a previous report that demonstrated that cationic gold nanorods were taken up into cells more efficiently than other nanoparticles.[27] Accordingly, it is noteworthy that the surface chemistry of nanoparticles considerably affects the cellular uptake as well as the size of nanoparticles.

Figure 6 exhibits TEM images of SK-BR-3 cells incubated with 10 μg mL^{-1} HNPs with different diameters. From the images, it could be considered that the cells ingested a relatively large amount of particles and that the cells retained cellular morphology without damage. The majority of particles seem to be confined inside cells that are distributed across the cytoplasm, but which did not cross into the nucleus. Within the cytoplasm, the nanoparticles appeared to be located in vesicles. Figure 6 shows that the number of nanoparticles per cell is related to the diameter of the HNPs.

In the case of J774A.1, similar results were observed that intercellular HNPs spread in the cytoplasm and demonstrated size-dependent uptake (Figure 7). From the images, the intercellular HNPs retained their shapes in the both cells. Furthermore, the cellular uptake of the surface-modified HNPs was also shown in Figure 6 and Figure 7. The amount of intercellular A-HNP50 was obviously larger compared with C-HNP50 and M-HNP50. This surface dependent behavior could be explained by electrostatic repulsion between nanoparticles and cell membrane.[28] Furthermore, this result expands to apply to modulating the efficiency of drug delivery with tunable internalization. It has been reported

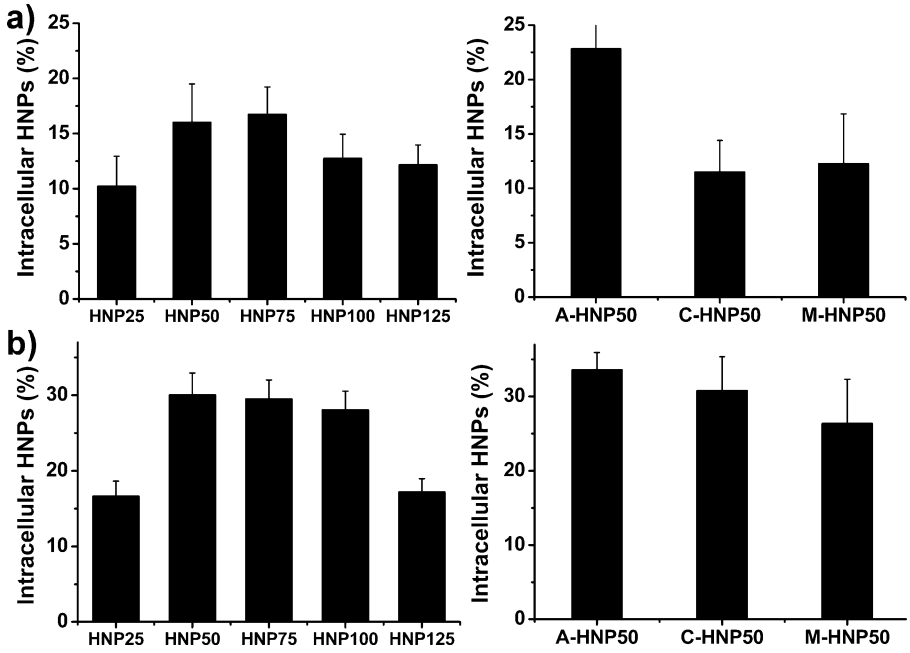

Figure 5. Quantification histogram of HNP-internalized (a) SK-BR-3 and (b) J774A.1 cells determined by ICP measurement.

that cellular uptake plays a pivotal role in the alteration of various cellular functions.[29] Therefore, the toxicity of HNP-treated cells should be investigated in order to verify the correlation between cellular uptake efficiency and toxicity.

The flow cytometry analyses (Figure 3) did not distinguish between nanoparticles in the cell and those attached outside to the cell membrane. Therefore, we calculated the number of the HNPs in the cells using software based on 10 cells in the TEM images. The calculated values were summarized in Figure 8. Intracellular HNPs increased with a decrease in the size of HNPs. The number of the intracellular HNP25 was more than 15−47 times bigger than that of the intracellular HNP125. In addition, HNPs with positive charge exhibited the highest efficiency, followed by neutral and then negative charge. Interestingly, the amount of the intracellular A-HNP50 was similar to that of the intracellular HNP25. It was considered that the surface charge of nanoparticles was an important factor of the uptake into cells as well as the diameter of nanoparticles.

Figure 9 represented the graphs of intracellular HNP weights. The weight of intracellular HNPs increased with increasing particle size except HNP100, while the intracellular particle numbers decreased with increasing particle size. This is because the particle volume increased with the radius cubed. This result was not consistent with the weight determined by ICP measurement because the ICP results showed the uptake ratio based on cellular Ti amount and loading Ti amount. In the case of surface functionalization, cationic surface (A-HNP50) showed the highest uptake amount, while neutral surface and anionic surface (M-HNP50 and C-HNP50) revealed a relatively lower amount than cationic surface.

As shown in Figure 8, the highest rank at the "number" was HNP25, but the lowest rank was HNP125. The number of internalized HNPs was inversely proportional to the particle size. Furthermore, the highest uptake for weight per cell was HNP125 and A-HNP50 (Figure 9). The highest value of "macromolecule carrying capacity" (MFI value per cell) was the HNP50 (Supporting Information, Figure S1). These results may provide the information about the best uptake size for bioapplications such as drug delivery and bioimaging.

Cell Viability. The cell viability with the HNPs was determined *in vitro* using alveolar macrophage J774A.1 cell lines (Figure 10). Alveolar macrophages protect the body *via* phagocytosis against airborne nanomaterials through a respiratory route.[30] As a result, nanotoxicity investigation of alveolar macrophage cells could be suitable for comprehending pulmonary nanotoxicology. To evaluate the number of viable cells, the highly sensitive luminescence-based assay was performed based on the quantification of the adenosine triphosphate (ATP) concentration. As shown in Figure 10, the ATP production of the HNPs represented a size- and concentration-dependent decrease on macrophages. Interestingly, the ATP contents of HNP25-treated cells were slightly larger than those of HNP50, which was correlated to the uptake efficiency of the HNPs. It can be considered that the cell viability of the HNPs was related to their cellular uptake. This was consistent with the findings of Y. Yuan *et al.* that discovered antitumor activity and adverse effects of hydroxyapatite nanoparticles were in order of 45-nm > 26-nm > 78-nm > 175-nm.[31] In addition to size, cationic HNPs (A-HNP50) with amine attachment revealed a high rate of toxicity in J774A.1 cells. Nonetheless, the cell viability of anionic and neutral HNPs (C-HNP50 and M-HNP50) relatively in-

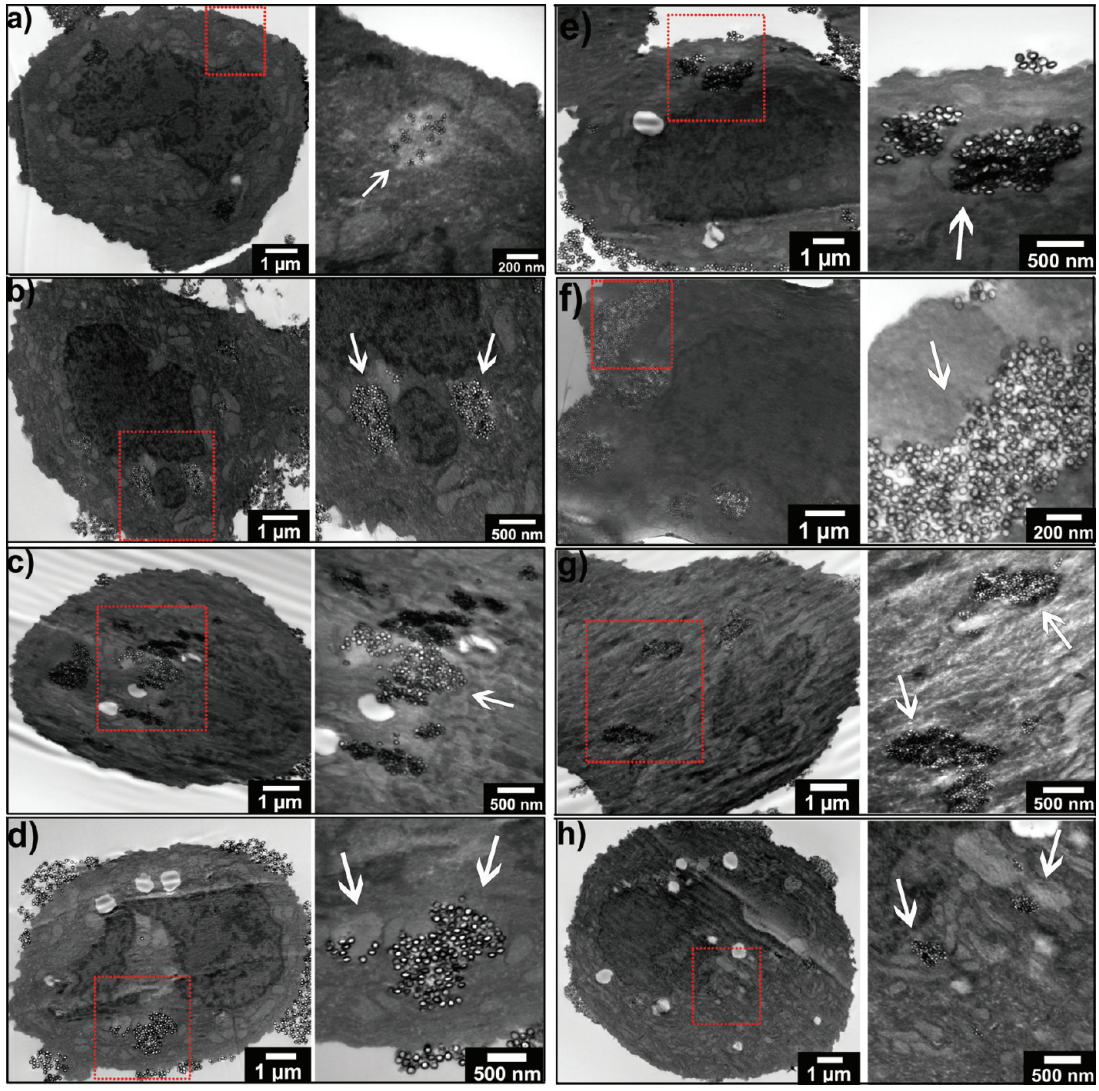

Figure 6. TEM images of HNP-internalized SK-BR-3 cells (right: corresponding magnified TEM images that red boxes indicate): (a) HNP25, (b) HNP50, (c) HNP75, (d) HNP100, (e) HNP125, (f) A-HNP50, (g) M-HNP50, and (h) C-HNP50. White arrows demonstrate HNPs.

creased in comparison with that of A-HNP50. This result was corroborated with a previous report that 60 nm NH_2-labeled polystyrene nanospheres were highly toxic in macrophage.[32] These cationic nanospheres were taken up into macrophages using the endosomal−lysosomal route, resulting in cell death caused by functional and structural mitochondrial changes.[32] The viabilities of the HNPs showed over 70% at a loading amount of 100 μg mL^{-1}. There was no significant drop in the viability to macrophages. These cell viability results are related to more immediate nanoparticle effects involving ROS production such as photoactivation and electronically active surfaces.[10] Consequently, it is necessary for evaluating the ROS generation of the HNPs toward macrophages compared with cellular viability.

Reactive Oxygen Species. It is known that a small size and large surface area could generate reactive oxygen species (ROS). The nanomaterial characteristics can culminate in ROS generation, which is currently the best-developed paradigm for nanoparticle toxicity. 2′,7′-Dichlorodihydrofluorescein diacetate (DCF-DA) staining methods were conducted for 24 h to investigate the role of ROS in cells with the HNPs. In the presence of ROS, DCF-DA is promptly oxidized to 2′,7′-dichlorodihydrofluorescein (DCF), resulting in the fluorescent intensity increment of cells. In Figure 11, ROS values were size-, functionality-, and concentration-dependent. Remarkably, the ROS production of the HNP50 on cells was more pronounced than that of other HNPs, and this result was corroborated by cellular uptake and viability results. Moreover, cationic surface (A-HNP50) represented higher ROS values compared with the anionic and neutral surface (C-HNP50 and C-HNP50). Under our experimental condition, 50-nm and cationic HNPs that are superior to phagocytosis, thus, exhibited the highest ROS production. The ROS production induced by nanomate-

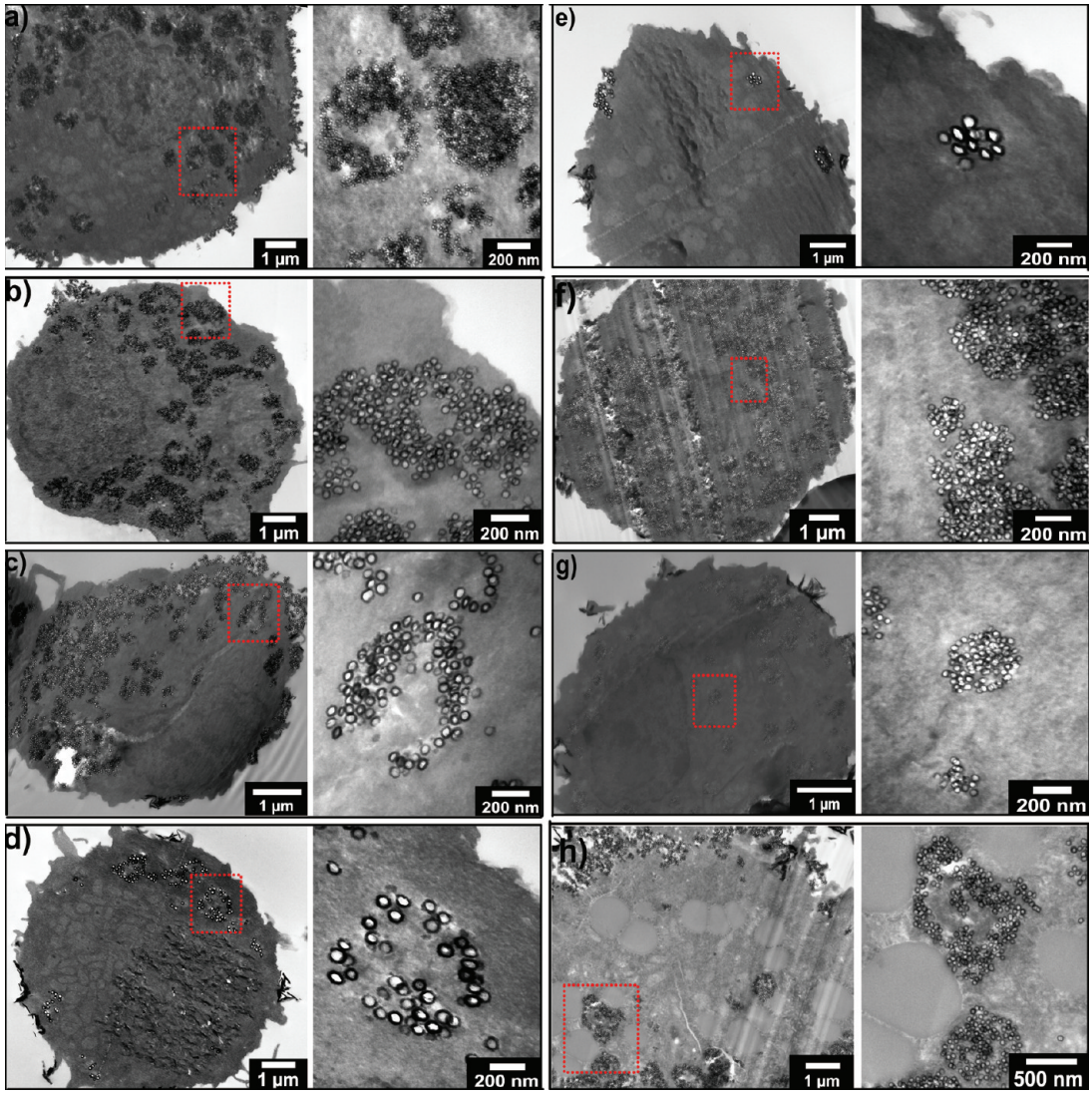

Figure 7. TEM images of HNP-internalized J774A.1 cells (right: corresponding magnified TEM images that red boxes indicate): (a) HNP25, (b) HNP50, (c) HNP75, (d) HNP100, (e) HNP125, (f) A-HNP50, (g) M-HNP50, and (h) C-HNP50.

rials can damage external (membrane) or internal (after nanomaterial uptake) cells and can also contribute to inflammation.[33] In addition, it is known that ROS production and following oxidative stress cause mitochondrial dysfunction, and this could contribute to initiate apoptosis.[34] Therefore, apoptosis in the HNP-treated cells should be evaluated to establish a relationship between oxidative stress and apoptosis.

Innate Immune Response of HNPs. A main purpose of phagocytic cells is their participation in inflammation as a major part of the body's immune mechanism. The in-

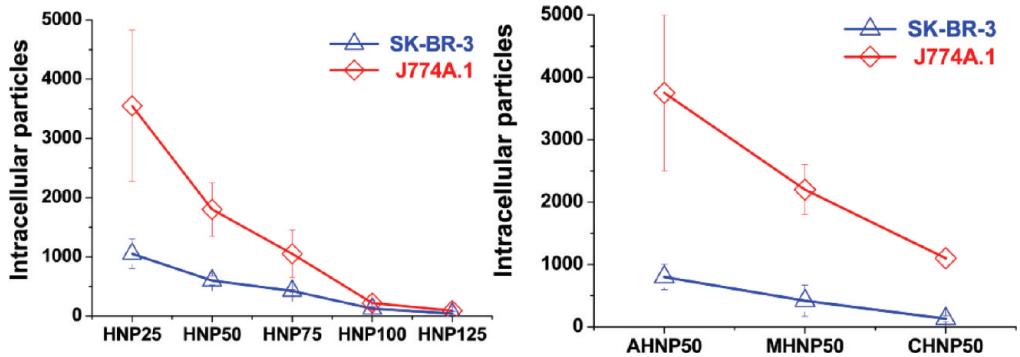

Figure 8. Counted intracellular HNPs in SK-BR-3 and J774A.1 cells. The number of the HNPs in the cells was calculated by using software based on 10 cells in the TEM images. Average particle numbers and standard errors were summarized.

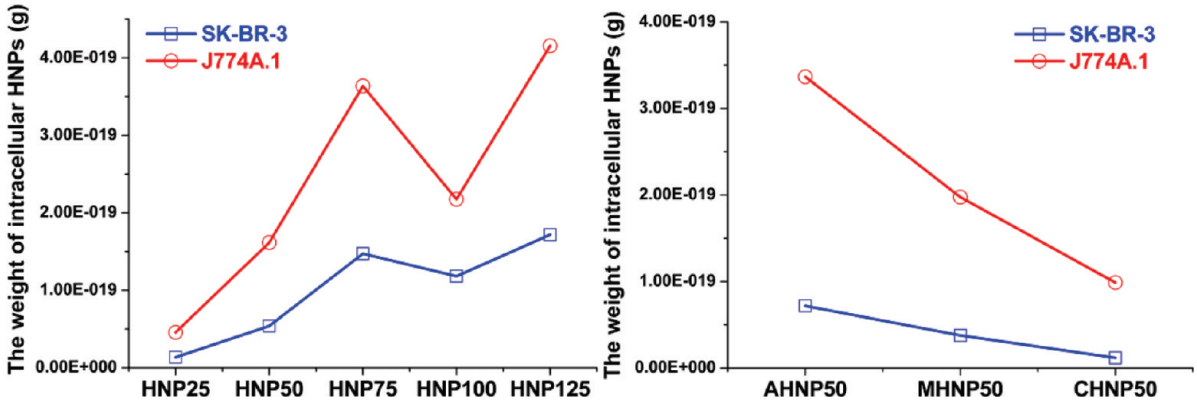

Figure 9. The weight of intracellular HNPs per SK-BR-3 and J774A.1 cell. The weight was calculated based on particle numbers in TEM images.

nate immune mechanism is motivated by the detection of nonself antigens including foreign particles, resulting in provoking various proinflammatory and cell-signaling molecules.[35] Therefore, the evaluation of proinflammatory response in alveolar macrophages treated with HNPs is of importance in nanotoxicological assessments. Furthermore, there is a direct relationship between the cell viability, ROS-generating capability, and inflammatory effects of nanoparticles as mentioned earlier. Cytokines play a key role in the proinflammatory response. The release of three cytokines known as interlukin-1 (IL-1), interlukin-6 (IL-6), and tumor necrosis factor (TNF-α) that are produced largely by phagocytes (*e.g.*, macrophages and neutrophiles) was involved in determining the immune response of HNPs. It was previously reported that TiO_2 nanoparticles generated these proinflammatory cytokine releases (5−20 times) in dendritic cells.[36] Under our experimental conditions, the proinflammatory response of macrophages to HNPs was investigated by analyzing the induction of the cytokines *via* real-time PCR of extracted RNA under lipopolysaccharides(LPS)-free conditions. Figure 12 reveals the inflammatory cytokine gene expression of J774A.1 macrophages treated with the 25

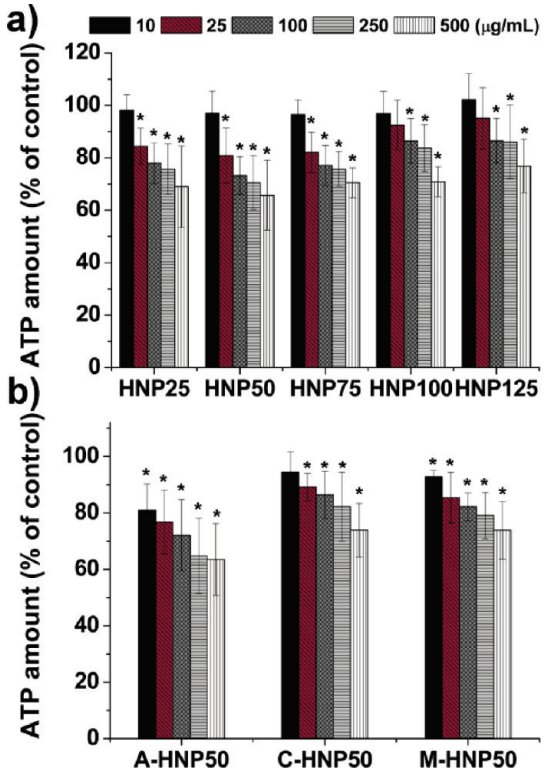

Figure 10. Viability of J774A.1 treated with HNPs, which was determined by the amount of ATP in the cells. J774A.1 was incubated with HNPs as a function of (a) diameters and (b) surface functionalities for 24 h. Values exhibit mean ± SD, and each experiment was performed in triplicate. The asterisk (*) denotes a statistically significant difference from a control exposed to HNPs ($P < 0.05$).

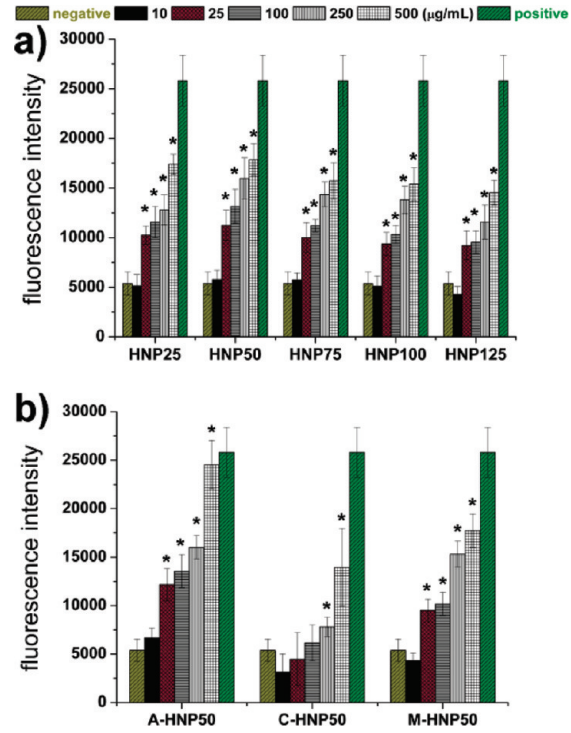

Figure 11. ROS production by J774A.1 cells after incubation with HNPs as a function of (a) diameters and (b) surface functionalities for 24 h. H_2O_2 (0.02%) was used as positive control. Values exhibit mean ± SD, and each experiment was performed in triplicate. The asterisk (*) denotes a statistically significant difference from control exposed to HNPs ($P < 0.05$).

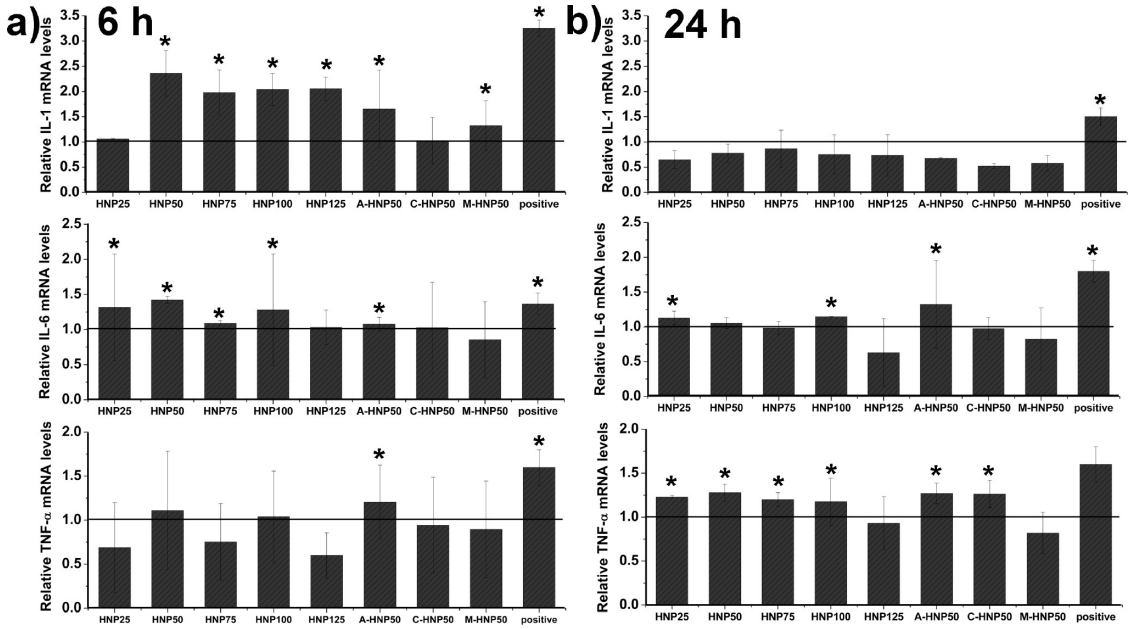

Figure 12. Expression of IL-1, IL-6, and TNF-α in J774A.1 macrophages incubated with culture medium containing HNPs at 25 μg mL^{-1} for (a) 6 h and (b) 24 h. Positive control was treated with LPS (25 ng mL^{-1}). Values exhibit mean ±SD, and each experiment was performed in triplicate. The asterisk (*) denotes a statistically significant difference from negative control ($P < 0.05$).

μg mL^{-1} HNPs for short-term (6 h) to long-term (24 h). The induction of IL-1 mRNA expression was observed after 6 h-treatment with HNPs, but not after 24 h-treatment. In contrast, the TNF-α mRNA induction was more prominent after 24 h of HNP treatment. All HNPs did not cause considerable increase in the cytokine gene expression compared to LPS (25 ng mL^{-1}). The cationic surface (A-HNP50) was more effective for induction of IL-1, IL-6, and TNF-α than the anionic and neutral surfaces. The toxicity of cationic particles was demonstrated when polycationic paint polymers induced pulmonary injury in rats and hamsters after tracheal instillation or inhalation exposure.[37] With respect to nanoparticle diameter, HNP50 exhibited the highest induction of IL-1, IL-6, and TNF- α after 6 h of incubation compared with HNPs of other sizes. It is noteworthy that these results are consistent with the effects of the HNPs on cell viability, uptake, and ROS generation. Judging from these data, the innate immune response of macrophages treated with HNPs also shows the dependence on size and surface functionality.

Apoptosis and Necrosis. Apoptosis and necrosis are considered as the most preferred responses among various mechanisms for investigating cell death.[38] Annexin V (aV) that was easily reacted with phosphatidylserin (PS) was used as a marker of apoptosis. Propidium iodide (PI), which was utilized to detect plasma membrane integrity, was employed for recognizing necrotic cell death. To quantify the amount of different cell deaths, aV and PI assays were conducted by FACSCalibur flow cytometry. A statistical value was acquired from the dot plots using WinMDI software, based on the percentages of aV−/PI− (viable cells), and those with aV−/PI+ (necrotic cells), aV+/PI− (apoptotic cells), and aV+/PI+ (late apoptotic cells). The above-mentioned results are summarized in Figure 13. After

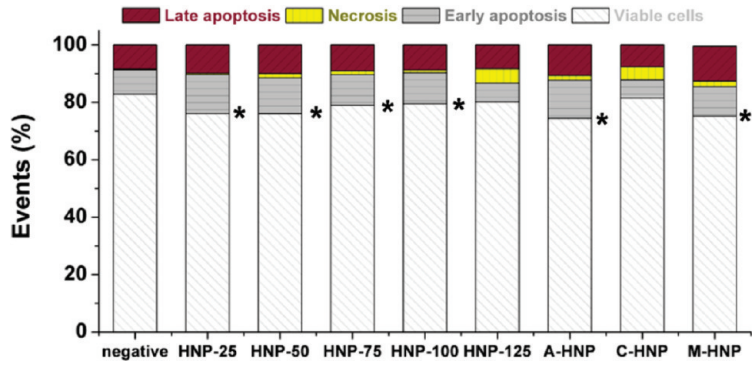

Figure 13. Apoptosis and necrosis ratio obtained from annexin V and PI staining. J774A.1 was incubated with HNPs (25 μg mL^{-1}) for 24 h. Each experiment was performed in triplicate. The asterisk (*) denotes a statistically significant difference from control exposed to HNPs ($P < 0.05$).

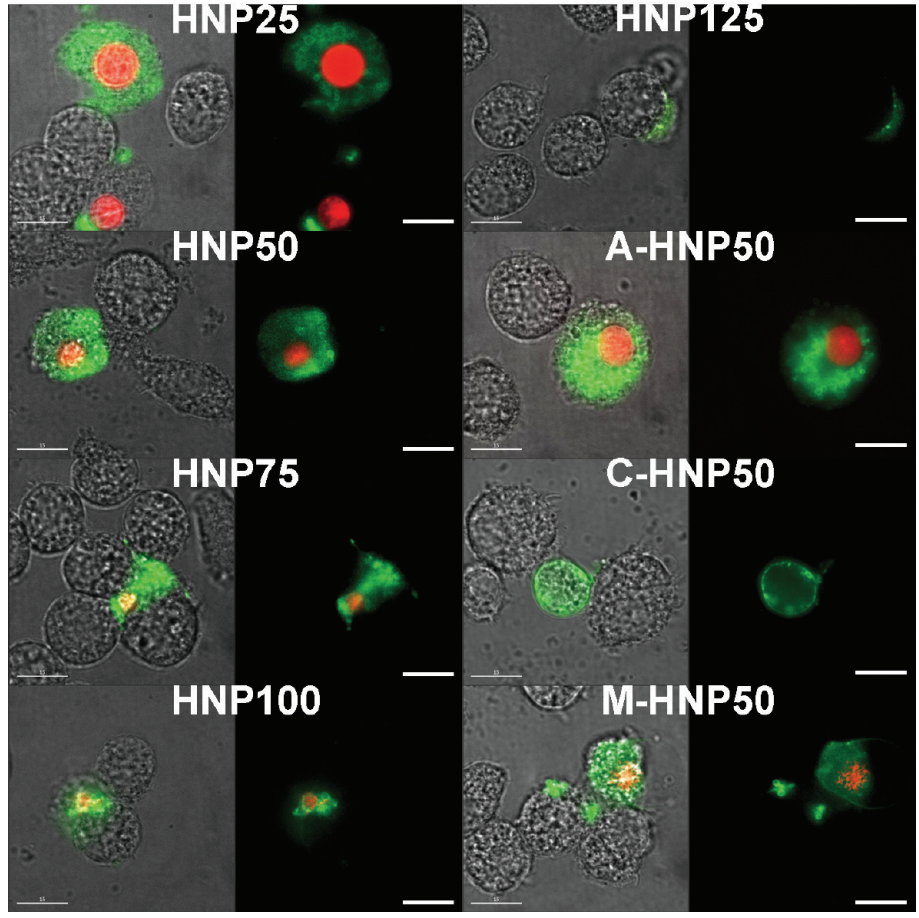

Figure 14. Live cell DIC and fluorescent images of HNP-treated J774A.1 cells (25 μg mL^{-1}). DIC images were taken at the same time corresponding to the cells. Green (aV) means apoptosis, red (PI) means necrosis. Scale bars = 15 μm.

manipulating the data for apoptotic and necrotic cells, a viability decrease from 83 (control) to 80, 79, 79, 76, and 76 was observed for J774A.1 treated with HNP125, HNP100, HNP75, HNP50, and HNP25, respectively, where the decreased viability mainly involved early apoptosis. In the case of the surface modification, a decrement in viable cells from 83 (control) to 81, 75, and 74 was observed in J774A.1 treated with C-HNP50, M-HNP50, and A-HNP125, respectively, where early apoptosis affected mostly decreasing the viability of J774A.1. Although the mechanism of J774A.1 apoptosis was not fully understood, the apoptosis was thought to be caused by perturbing proton pump activity.[31] This led to lysosomal rupture or damage to the mitochondrial outer membrane, resulting in the release of pro-apoptotic factors.

Figure 14 displays live cell microscopic images of cells treated with the HNPs in which the cells were stained with aV and PI. Unstained cells define viable cells, and green fluorescent labels/red fluorescent labels are classified as early apoptotic cells/necrotic cells. Dual stained cells are categorized as late apoptotic cells. In Figure 14, green and red fluorescent dots increased in inverse proportion to the size of HNPs, and green and red fluorescent dots increased in A-HNP50-internalized macrophages as compared with C-HNP50 and M-HNP50. Some cells treated with HNPs were altered with their own shapes mainly due to disorders in cytoskeletal functions. Taking these facts into account, the apoptosis and necrosis in HNP-internalized macrophages were size-dependent and surface functionality-dependent, which agrees with other experimental results. It is considered that the toxicity of nanoparticles is related to their cellular internalization efficiency. Accordingly, 50-nm cationic hollow nanoparticles showed the most harmful effect for both cell lines in every toxicity evaluation as well as representing the highest uptake efficiency. Although *in vitro* toxicity research cannot exhibit accurate toxicological analysis linked with *in vivo* toxicity, these studies may be expanded to allow the investigation of cellular nanotoxicity pathways as well as the interaction between nanomaterials and cells.

CONCLUSION

Monodisperse hollow nanoparticles with diameters of 25, 50, 75, 100, and 125 nm were fabricated by a dissolution and redeposition method, and surface-modified with functional groups of amine, carboxylate, and methylene. We systematically investigated the key factors affecting cellular uptake, nanotoxicity, and im-

mune response of HNPs with size- and functionality-dependence in human breast cancer SK-BR-3 and mouse alveolar macrophage J774A.1 cells. The number of cellular uptake of HNPs was in inverse proportion of HNP size while the weight of intercellular HNPs was in the order of HNP75 > HNP50 ≥ HNP100 > HNP125 > HNP25. The highest value of mean fluorescence intensity was HNP50. In the case of surface functionality, the cellular uptake orders were A-HNP50 > M-HNP50 and C-HNP50 in the number and weight mainly due to the size effect and the positive charge of HNPs. In addition the cellular uptake, the ATP production, apoptosis, and ROS revealed size- and surface functionality-dependent toxicity of HNPs toward macrophages. Among the various HNPs, 50-nm cationic HNPs represented the most harmful to macrophages. The innate immune response also showed that J774A.1 treated with 50-nm cationic HNPs generated the highest cytokine release of IL-1, IL-6, and TNF-α compared with other HNPs. In addition, this methodology may provide the systematical investigation for size and functionality parameters of HNPs with respect to cellular uptake and nanotoxicity and the application of various HNPs to biomedical fields.

MATERIALS AND METHODS

Synthesis of HNPs. In a typical synthesis of silica−titania hollow nanoparticles, silica nanoparticles were first prepared according to the Stöber method. For preparing silica nanoparticles, 2.3 mL of tetraethyl orthosilicate (TEOS; Aldrich, St. Louis, MO) was added to the mixture solution of ethanol (60 mL), ammonium hydroxide solution (3.0 mL), and water (1.0 mL). Especially, a sol−gel reaction was performed for 6 h under various temperature conditions (55, 50, 40, 35, and 20 °C) for synthesizing silica nanoparticles and subsequent 25-nm, 50-nm, 75-nm, 100-nm, and 125-nm hollow nanoparticles. Then, 2.9 mL of TTIP (Aldrich, St. Louis, MO) was introduced in the above-mentioned solution for the titania-coated layer, and the resulting solution was stirred for 6 h at room temperature. The prepared silica−titania core−shell nanoparticles were redispersed in 10 mL of sodium hydroxide solution (1.0 M) and then stirred for 3 h at room temperature. After the reaction, synthesized hollow nanoparticles were collected by centrifugation (10000 rpm, 30 min). Transmission electron microscopy (TEM) images were obtained with a JEOL EM-2000 EX II microscope. The surface charge (zeta potential) and size distribution of HNPs were measured by ELS-8000 (Otsuka Electronics, Japan) utilizing an ELS. The nanoparticles were dispersed in aqueous solutions at a concentration of 10 μg mL^{-1}, and then sonicated for 3 min before measuring zeta potential and size distribution.

Surface Modification of HNPs. The proper silanes were used in the surface modification of HNPs in order to explore the effect of surface functionalities. The silane coupling agents (0.5 wt %) including 3-aminopropyltriethoxysilane for amine treatment (A-HNP50), carboxylethylsilanetriol sodium salt for carboxylate treatment (C-HNP50), and 3-methacryloxypropyltrimethoxysilane for methylene treatment (M-HNP50) were introduced into ethanol solution with HNPs. The mixture solutions were magnetically stirred overnight and then thoroughly washed to gain surface-modified HNPs with different functionality.

Cell Culture and Experimental Overview. Human breast cancer SK-BR-3 and mouse alveolar macrophage J774A.1 cell lines were purchased from American Type Culture Collection (ATCC, Manassas, VA). SK-BR-3 and J774A.1 were cultured with RPMI-1640 medium, with 10% fetal bovine serum, 1% penicillin-streptomycin solution, 300 mg L^{-1} L-glutamine, 25 mM sodium bicarbonate, and 25 mM 4-(2-hydroxyethyl)-1-piperazine ethanesulfonic acid (HEPES). The cell lines were incubated in a 5% CO_2 incubator at 37 °C and 100% humidity. Cells were placed in 75T flask and maintained between 1×10^5 and 1×10^6 cells mL^{-1} of medium. In addition, all experiments were conducted in a clean atmosphere to avoid the endotoxin contamination which might affect to the toxicity tests of the HNPs. Stock solutions of different HNPs (10 mg mL^{-1}) were diluted to the required concentrations (10, 25, 100, 250, 500 μg mL^{-1}).

Quantification of Incorporated HNPs into Cells. To incorporate HNPs into cells, the surfaces of the HNPs were modified using 3-aminopropyl-trimethoxysilane. And then, amino-modified HNPs with different diameters were tagged with FITC (Sigma, St. Louis, MO). Cells were seeded at a density of 2000 cells per well, in 8-well Lab-TekTM II Chambered Coverglass (Nunc, Thermo Fisher Scientific) and treated with FITC-tagged HNPs (10 μg mL^{-1}). After 24 h incubating, the live cells were imaged by DeltaVision RT imaging system (Applied Precision, Issaquah) with controlled temperature (37 °C) and CO_2 concentration (5%). To obtain live cell images, a 40× oil immersion objective was employed with Cascade II EMCCD camera. A λ_{ex} of 494 nm was used for fluorescence imaging of cells treated with FITC-tagged HNPs.

Cellular uptake measurement was carried out *via* flow cytometric measurement. Cells were seeded in a 6-well plate (Falcon, USA). After 25 μg mL^{-1} of FITC-tagged HNPs treatments for 24 h, the medium was aspirated and cells were washed to eliminate floating HNPs. Cells were collected and centrifuged. The cells were then rinsed with 0.1 M phosphate buffered saline (PBS) and resuspended in PBS at the concentration 1×10^6 cells mL^{-1}. Flow cytometry analysis was performed with FACSCalibur flow cytometry at an emission wavelength of 530 nm for FITC.

ICP (JP/ICPS-7500, Shimdzu) measurement was used for quantifying HNPs incorporated into cells. The cells were seeded in a 6-well plate and treated with 25 μg mL^{-1} of the HNPs for 24 h. The cells were washed and collected. The cells were resuspended in distilled water and centrifuged again. After the cells were dried overnight, 48−51 wt % HF was added to allow dissolution of HNPs. Then, 2 wt % HNO_3 in aqueous solution was added to allow dissolution of the cells with ultrasound. The mass of HNPs in the cells was measured by detecting the titanium concentration with ICP. The weight of intracellular HNPs based on particle numbers in TEM images was calculated by using the following formula:

$$\text{intercellular HNP weight} = \frac{4}{3}\pi(R^3 - r^3)\rho n$$

where R is the outside radius of the HNP, r is the inside radius, ρ is the density of the HNPs, and n is the average number of intracellular HNPs.

TEM of HNP-Treated Cells. The cellular uptake of the HNPs into SK-BR-3 and J774A.1 cell lines were observed with TEM (JEM-2000EXII, JEOL). SK-BR-3 and J774A.1 cells were cultured in Lab-Tek II chamber slides until 80% confluence. After incubation with 10 μg mL^{-1} HNPs for 24 h, cells were prefixed with 2% paraformaldehyde and 2% glutaraldehyde at 4 °C for 4 h. After being washed with 0.05 M cacodylate buffer, cells were postfixed with 1% osmiumtetraoxide at 4 °C for 2 h, washed with distilled water, and then stained with 0.5% uranyl acetate at 4 °C. The cells were dehydrated through a series of ethyl alcohol concentrations (30%, 50%, 70%, 80%, 90%, 100%, 100%, and dry alcohol). Then, the cells were treated with propylene oxide followed by 1:1 propylene oxide:spurr's resin for 2 h. The cells were infiltrated in spurr's resin at 70 °C for 24 h and ultramicrotome was conducted. Then, the samples were observed with the TEM at 150 kV.

Cell Viability. The viability of HNP-treated J774A.1 was measured using CellTiter glow luminescent cell viability assay (Promega, Madison, WI). This assay is able to estimate the number of viable cells based on quantification of the ATP concentra-

tion in cells. This assay detects a luminescent signal in proportion to the amount of ATP present in cells. The luminescence comes from the change of beetle luciferin to oxyluciferin by a thermostable luciferase in the presence of ATP. The experiments were performed in a 96-well plate. For the assay, 5000 cells per well were plated and treated with different concentrations of HNPs (10, 25, 100, 250, and 500 μg mL^{-1}) for 24 h. The protocol of this assay followed manufacturer's instructions. The luminescence of the HNP-treated cells were detected by Victor³ Multilabel Readers at an emission wavelength of 595 nm.

Reactive Oxygen Species. The generation of ROS was evaluated by using DCF-DA (Invitrogen, Grand Island, NY) staining. In the presence of a H_2O_2 or hydroxyl radicals, DCF-DA is converted to DCF, a highly fluorescent derivative. The ROS assay was performed by supplier's instructions. Approximately 5000 J774A.1 cells incubated with HNPs (10, 25, 100, 250, and 500 μg mL^{-1}) for 24 h in 96-well plate were treated with 10 μM DCF-DA for 20 min at 37 °C. H_2O_2 (0.02%) was used as a positive control. Cells were analyzed by Victor³ Multilabel Readers at an emission wavelength of 535 nm.

RNA Extraction and Real-Time PCR Analysis. Cells (1×10^6 cells) with HNP (25 μg mL^{-1}) treatment were collected at 6 and 24 h treatments and the total RNA was extracted by disrupting cells in 1.0 mL Trizol reagent (Invitrogen, Carlsbad, CA) after gentle shaking for 10 min. Chloroform was added in the solution at room temperature for 10 min and centrifuged at 12000*g* at 4 °C for 15 min. The upper layer (aqueous phase) was moved into 0.5 mL of isopropyl alcohol and incubated for 30 min, then centrifuged at 12000*g* at 4 °C for 20 min. The supernatant was aspirated, and the pellet was rinsed with 1 mL of cold 75% ethanol/diethyl pyrocarbonate (DEPC) solution. The pellet was centrifuged and dried for 10 min. The extracted RNA that was diluted 40 times was determined using NanoDrop 2000 (Thermo Scientific, Wilmington, DE) at 260 and 280 nm in order to verify the purity of the extracted RNA. Afterward, the extracted RNA was reverse-transcribed to cDNA. Briefly, cDNA synthesis and amplification *via* real-time PCR were conducted using the SuperScript First-Strand Synthesis System for real-time PCR (Invitrogen, Carlsbad, CA) as per supplier's instructions. Each sample for real-time PCR analysis contained 100 ng of cDNA, SYBR Premix Ex Taq (Takara, Shiga, Japan), and 0.2 μM of each custom primer. The β-actin was employed as a reference housekeeping gene. LPS (Sigma, St. Louis, MO) was used for a positive control. The cDNA was used for detecting the expression of IL-1, IL-6, and TNF-α cytokines. The reactions were performed using the following primer pairs:

5′-CCC AAG CAA TAC CCA AAG AAG AAG-3′ and 5′-TGT CCT GAC CAC TGT TGT TTC C-3′ for IL-1, 5′-TTC CAT CCA GTT GCC TTC TTG-3′ and 5′-TCA TTT CCA CGA TTT CCC AGA G-3′ for IL-6, 5′-CGA GTG ACA AGC CTG TAG CC-3′ and 5′-TTG AAG AGA ACC TGG GAG TAG AC-3′ for TNF-α, and 5′-TCC TGT GGC ATC CAC GAA ACT-3′ and 5′-GGA GCA ATG ATC CTG ATC TTC-3′ for β-actin.

The PCR amplification and real-time fluorescence quantification were performed by using LightCycler 480 plate-based real-time PCR System (Roche Appiled Science, Penzberg, Germany). The cDNA was denatured at 95 °C for 5 min. This was followed by amplification of the target DNA through 40 cycles of denaturation at 95 °C for 20 s and elongation at 60 °C for 20 s and 72 °C for 20 s.

Apoptosis and Necrosis. Annexin V and PI staining was conducted to differentiate apoptosis from necrosis induced by HNPs. After an apoptotic stimulus, PS moves from the inner leaflet of the plasma membrane to the outer leaflet of plasma membrane, and the secreted amount of PS indicates the amount of apoptosis.[39] Cells were counterstained with PI, a nonpermeable stain for nucleic acids, to recognize necrotic cell death. Annexin V assay provides a simple and effective method to detect apoptosis at a very early stage. Annexin V conjugated to AlexaFluor488 (aV; Vybrant apoptosis assay kit, Molecular Probes, Invitrogen, Grand Island, NY) makes the observation possible by an image restoration microscope. PI stains dead cells with red fluorescent, binding to the nucleic acids in the cells. In addition, aV stains apoptotic cells with green fluorescent. Cells were spread at a density of 3000 cells per well, in 8-well Lab-Tek II Chambered Coverglass (Nunc, Thermo Fisher Scientific, USA) and treated with HNPs (25 μg mL^{-1}). After 24 h incubation, the aV and PI staining were performed as per manufacturer's instructions. Live cell imaging was obtained by DeltaVision RT imaging system with temperature (37 °C) and CO_2 (5%) control. aV was excited with a 488 nm laser line and PI was excited by a 543 nm laser line.

Apoptosis and necrosis quantification was conducted using aV and PI staining followed by flow cytometry analysis. Approximately 1×10^5 cells were seeded in 6-well plate (Falcon, USA). After 25 μg HNP treatments for 24 h, the aV and PI staining was carried out as per manufacturer's instructions. Flow cytometry analysis was carried out using FACSCalibur flow cytometry (Becton Dickinson, USA) at an emission wavelength of 530 nm for aV and 585 nm for PI. Statistical data was obtained from the dot plots using WinMDI software.

Statistical Analysis. Measured values were expressed as mean_standard deviation. Results in the above-mentioned assays were evaluated by means of one-way analysis of variance (ANOVA) with a Duncan's test for the multiple comparisons; $p < 0.05$ is judged as statistically significant.

Acknowledgment. This research was supported by the Center for Advanced Materials Processing (CAMP) under the 21st Century Frontier R&D Programs of the Ministry of Commerce, Industry, and Energy (MOCIE), and WCU (World Class University) program through the National Research Foundation of Korea funded by the Ministry of Education, Science and Technology (R31-10013).

Supporting Information Available: The zeta potentials (ξ) of surface-functionalized HNPs, mean-fluorescence intensity (MFI) of HNP-treated cells, and MFI per single HNP. This material is available free of charge *via* the Internet at http://pubs.acs.org.

REFERENCES AND NOTES

1. Yoon, H.; Jang, J. Conducting-Polymer Nanomaterials for High-Performance Sensor Applications: Issues and Challenges. *Adv. Funct. Mater.* **2009**, *19*, 1567–76.
2. Jang, J. Conducting Polymer Nanomaterials and Their Applications. *Adv. Polym. Sci.* **2006**, *199*, 189–259.
3. Oh, W. -K.; Yoon, H.; Jang, J. Size Control of Magnetic Carbon Nanoparticles for Drug Delivery. *Biomaterials* **2010**, *31*, 1342–8.
4. Xia, T.; Kovochich, M.; Liong, M.; Meng, H.; Kabehie, S.; George, S.; Zink, J. I.; Nel, A. E. Polyethyleneimine Coating Enhances the Cellular Uptake of Mesoporous Silica Nanoparticles and Allows Safe Delivery of siRNA and DNA Constructs. *ACS Nano* **2009**, *3*, 3273–86.
5. Tao, Z.; Toms, B.; Goodisman, J.; Asefa, T. Mesoporous Silica Microparticles Enhance the Cytotoxicity of Anticancer Platinum Drugs. *ACS Nano* **2010**, *4*, 789–94.
6. Nel, A. E.; Mädler, L.; Velegol, D.; Xia, T.; Hoek, E. M. V.; Somasundaran, P.; Klaessig, F.; Castranova, V.; Thompson, M. Understanding Biophysicochemical Interactions at the Nano−Bio Interface. *Nat. Mater.* **2009**, *8*, 543–57.
7. AshaRani, P. V.; Mun, G. L. K.; Hande, M. P.; Valiyaveettil, S. Cytotoxicity and Genotoxicity of Silver Nanoparticles in Human Cells. *ACS Nano* **2009**, *3*, 279–90.
8. Verma, A.; Stellacci, F. Effect of Surface Properties on Nanoparticle−Cell Interactions. *Small* **2010**, *6*, 12–21.
9. Xia, T.; Kovochich, M.; Liong, M.; Mädler, L.; Gilbert, B.; Shi, H.; Yeh, J. I.; Zink, J. I.; Nel, A. E. Comparison of the Mechanism of Toxicity of Zinc Oxide and Cerium Oxide Nanoparticles Based on Dissolution and Oxidative Stress Properties. *ACS Nano* **2008**, *2*, 2121–34.
10. Nel, A.; Xia, T.; Mädler, L.; Li, N. Toxic Potential of Materials at the Nanolevel. *Science* **2006**, *311*, 622–7.
11. Nativo, P.; Prior, I. A.; Brust, M. Uptake and Intracellular Fate of Surface-Modified Gold Nanoparticles. *ACS Nano* **2008**, *2*, 1639–44.
12. Zhu, J.; Tang, J.; Zhao, L.; Zhou, X.; Wang, Y.; Yu, C. Ultrasmall, Well-Dispersed, Hollow Siliceous Spheres with Enhanced Endocytosis Properties. *Small* **2010**, *6*, 276–82.
13. Lou, X. W.; Archer, L. A.; Yang, Z. Hollow Micro-/Nanostructures: Synthesis and Applications. *Adv. Mater.* **2008**, *20*, 3987–4019.

14. You, J.; Zhang, G.; Li, C. Exceptionally High Payload of Doxorubicin in Hollow Gold Nanospheres for Near-Infrared Light-Triggered Drug Release. *ACS Nano* **2010**, *4*, 1033–41.
15. Yin, Y.; Rioux, R. M.; Erdonmez, C. K.; Hughes, S.; Somorjal, G. A.; Alivisatos, A. P. Formation of Hollow Nanocrystals through the Nanoscale Kirkendall Effect. *Science* **2004**, *304*, 711–4.
16. Jang, J.; Lee, K. Facile Fabrication of Hollow Polystyrene Nanocapsules by Microemulsion Polymerization. *Chem. Commun.* **2002**, 1098–9.
17. Zhang, T.; Ge, J.; Hu, Y.; Zhang, Q.; Aloni, S.; Yin, Y. Formation of Hollow Silica Colloids through a Spontaneous Dissolution-Regrowth Process. *Angew. Chem., Int. Ed.* **2008**, *47*, 5806–11.
18. Chen, Y.; Chen, H.; Guo, L.; He, Q.; Chen, F.; Zhou, J.; Feng, J.; Shi, J. Hollow/Rattle-Type Mesoporous Nanostructures by a Structural Difference-Based Selective Etching Strategy. *ACS Nano* **2009**, *4*, 529–39.
19. Fan, H. J.; Gösele, U.; Zacharias, M. Formation of Nanotubes and Hollow Nanoparticles Based on Kirkendall and Diffusion Processes: A Review. *Small* **2007**, *3*, 1660–71.
20. Wan, D.; Chen, H.-L.; Lin, Y.-S.; Chuang, S.-Y.; Shieh, J.; Chen, S.-H. Using Spectroscopic Ellipsometry to Characterize and Apply the Optical Constants of Hollow Gold Nanoparticles. *ACS Nano* **2009**, *3*, 960–70.
21. Zeng, H.; Cai, W.; Liu, P.; Xu, X.; Zhou, H.; Klingshirn, C.; Kalt, H. ZnO-Based Hollow Nanoparticles by Selective Etching: Elimination and Reconstruction of Metal-Semiconductor Interface, Improvement of Blue Emission and Photocatalysis. *ACS Nano* **2008**, *2*, 1661–70.
22. Kim, C.; Choi, M.; Jang, J. Nitrogen-Doped SiO_2/TiO_2 Core/Shell Nanoparticles as Highly Efficient Visible Light Photocatalyst. *J. Colloid Interface Sci.* **2010**, *11*, 378–82.
23. Park, S.-J.; Kim, Y.-J.; Park, S.-J. Size-Dependent Shape Evolution of Silica Nanoparticles into Hollow Structures. *Langmuir* **2008**, *24*, 12134–7.
24. Zhang, T.; Stilwell, J. L.; Gerion, D.; Ding, L.; Elboudwarej, O.; Cooke, P. A.; Gray, J. W.; Alivisatos, A. P.; Chen, F. F. Cellular Effect of High Doses of Silica-Coated Quantum Dot Profiled with High Throughput Gene Expression Analysis and High Content Cellomics Measurements. *Nano Lett.* **2006**, *6*, 800–8.
25. Huang, X.; Teng, X.; Chen, D.; Tang, F.; He, J. The Effect of the Shape of Mesoporous Silica Nanoparticles on Cellular Uptake and Cell Function. *Biomaterials* **2010**, *31*, 438–48.
26. Osaki, F.; Kanamori, T.; Sando, S.; Sera, T.; Aoyama, Y. A Quantum Dot Conjugated Sugar Ball and Its Cellular Uptake. On the Size Effects of Endocytosis in the Subviral Region. *J. Am. Chem. Soc.* **2004**, *126*, 6520–1.
27. Hauck, T. S.; Ghazani, A. A.; Chan, W. C. W. Assessing the Effect of Surface Chemistry on Gold Nanorod Uptake, Toxicity, and Gene Expression in Mammalian Cells. *Small* **2008**, *4*, 153–9.
28. Jiang, J.; Oberdörster, G.; Biswas, P. Characterization of Size, Surface Charge, and Agglomeration State of Nanoparticle Dispersions for Toxicological Studies. *J. Nanopart. Res.* **2009**, *11*, 77–89.
29. Polo, S.; Di Fiore, P. P. Endocytosis Conducts the Cell Signaling Orchestra. *Cell* **2006**, *124*, 897–900.
30. Bastús, N. G.; Sánchez-Tilló, E.; Pujals, S.; Farrera, C.; López, C.; Giralt, E.; Celada, A.; Lloberas, J.; Puntes, V. Homogeneous Conjugation of Peptides onto Gold Nanoparticles Enhances Macrophage Response. *ACS Nano* **2009**, *3*, 1335–44.
31. Yuan, Y.; Liu, C.; Qian, J.; Wang, J.; Zhang, Y. Size-Mediated Cytotoxicity and Apoptosis of Hydroxyapatite Nanoparticles in Human Hepatoma HepG2 Cells. *Biomaterials* **2010**, *31*, 730–40.
32. Xia, T.; Kovochich, M.; Liong, M.; Zink, J. I.; Nel, A. E. Cationic Polystyrene Nanosphere Toxicity Depends on Cell-Specific Endocytic and Mitochondrial Injury Pathways. *ACS Nano* **2008**, *2*, 85–96.
33. Mitchell, L. A.; Lauer, F. T.; Burchiel, S. W.; McDonald, J. D. Mechanisms for How Inhaled Multiwalled Carbon Nanotubes Suppress Systemic Immune Function in Mice. *Nat. Nanotechnol.* **2009**, *4*, 451–6.
34. Du, J.; Daniels, D. H.; Asbury, C.; Venkataraman, S.; Liu, J.; Spitz, D. R.; Oberley, L. W.; Cullen, J. J. Mitochondrial Production of Reactive Oxygen Species Mediate Dicumarol-Induced Cytotoxicity in Cancer Cells. *J. Biol. Chem.* **2006**, *281*, 37416–26.
35. Bastús, N. G.; Sánchez-Tilló, E.; Pujals, S.; Farrera, C.; Kogan, M. J.; Giralt, E.; Celada, A.; Lloberas, J.; Puntes, V. Peptides Conjugated to Gold Nanoparticles Induce Macrophage Activation. *Mol. Immunol.* **2009**, *46*, 743–8.
36. Schanen, B. C.; Karakoti, A. S.; Seal, S.; Drake III, D. R.; Warren, W. L.; Self, W. T. Exposure to Titanium Dioxide Nanomaterials Provokes Inflammation of an *in Vitro* Human Immune Construct. *ACS Nano* **2009**, *3*, 2523–32.
37. Hoet, P. H.; Gilissen, L.; Nemery, B. Polyanions Protect Against the *in Vitro* Pumonary Toxicity of Polycationic Paint Components Associated with the Ardystil Syndrome. *Toxicol. Appl. Pharmacol.* **2001**, *175*, 184–190.
38. Kang, B.; Mackey, M. A.; El-Sayed, M. A. Nuclear Targeting of Gold Nanoparticles in Cancer Cells Induces DNA Damage, Causing Cytokinesis Arrest and Apoptosis. *J. Am. Chem. Soc.* **2010**, *132*, 1517–9.
39. Vallhov, H.; Gabrielsson, S.; Strømme, M.; Scheynius, A.; Garcia-Bennett, A. E. Mesoporous Silica Particles Induce Size Dependent Effects on Human Dendritic Cells. *Nano Lett.* **2007**, *7*, 3576–82.